

Characterization of Heat-Affected Powder Generated during the Selective Laser Melting of 304L Stainless Steel Powder

Austin T. Sutton¹, Caitlin S. Kriewall², Ming C. Leu¹, Joseph W. Newkirk²

¹Department of Mechanical and Aerospace Engineering, Missouri University of Science and Technology, Rolla, MO 65409

²Department of Materials Science and Engineering, Missouri University of Science and Technology, Rolla, MO 65409

Abstract

The selective laser melting (SLM) process is an Additive Manufacturing (AM) technique that uses a laser to fuse successive layers of powder into near fully dense components. Due to the large energy input from the laser during processing, vaporization and instabilities in the melt pool occur causing the formation of condensate and laser spatter, collectively known as heat-affected powder. Since heat-affected powder settles into the powder bed, the properties of the unconsolidated powder may be altered compromising its reusability. In this study, characterization of 304L heat-affected powder was performed through particle size distribution measurements, x-ray diffraction, metallography, energy-dispersive spectroscopy mapping, and visualization of grain structure with the aid of a focused-ion beam. The results show morphological, microstructural, and surface chemistry differences between the starting powder and heat-affected powder formed during processing which aid in the understanding of laser spatter and condensate that form in the SLM process.

Introduction

Powder-bed fusion refers to a subset of Additive Manufacturing (AM) processes that bond powder layers in a sequential manner for the production of three-dimensional components directly from Computer-Aided Design (CAD) files [1]. Among this class of manufacturing techniques is the selective laser melting (SLM) process where a laser scans across a powder-bed melting and consolidating particles to form parts that approach theoretical density [2,3]. The layer thickness is often no more than 70 μm facilitating the construction of fine features and, thus, overall geometrical complexity. Consequently, SLM has attracted a significant amount of interest from a wide variety of areas involving biomedical, aeronautical, and automotive applications.

A large portion of the research conducted in SLM has been focused on adjusting laser process parameters for manufacturability of a variety of materials such as Ti-6Al-4V [4,5], 316/316L stainless steel [6,7], and IN718 [8,9]. Typically, these variables include the laser power, scan speed, and hatch spacing for which an optimal combination is found to minimize porosity. Other work in SLM has been centered on the interaction of the laser beam with the powder-bed through heat and fluid flow simulations for insight into melt pool formation and cooling rates [10–12]. In general, it is found that the melt pool experiences high thermal gradients giving rise to strong Marangoni convection currents, which play a large role in the wetting behavior of the melt on the previously solidified layer. Adding to the complexity of the process is the dependence of the melt pool wettability on the oxygen content where the balling phenomenon can be induced as

a result of the presence of oxides [13,14]. The onset of balling indicates a lack of wetting and can ultimately cause the formation of porosity and possible damage to the recoating mechanism. Results from simulations also show that the melt pool experiences a high degree of superheat leading to vaporization of material and subsequent ejection of material. Rapid vaporization of material is known to cause melt pool instabilities by providing a large upsurge of vertical momentum in the melt pool causing molten material to be ejected in the form of laser spatter [15–17]. Moreover, vaporized material that escapes the melt pool rapidly solidifies in the chamber atmosphere causing the formation of nano-particles, more commonly known as condensate, that coat the inside of the build chamber during the SLM process. If generated in excess or not adequately removed, condensate can lead to attenuation and defocusing of the laser beam causing pore formation due to a lack of fusion [18–21].

The collection of both laser spatter and condensate is hereby referred to as heat-affected powder as it is formed under high temperature conditions originating from the melt pool. In SLM, studies regarding laser spatter characterization and the potential consequences of its formation on part quality are seldom. Simonelli et al. [22] characterized the spatter formed from 316L stainless steel, Al-Si10-Mg, and Ti-6Al-4V generated during SLM. It was found that laser spatter is not only comprised of particles much larger than the base powder, but is also chemically different as a result of oxidation on the outer surfaces of the particles. Liu et al. [19] also found that laser spatter generated from processing 316L was large with some particles having an approximate diameter of 400 μm . Although typical procedures involve sieving of used powder to eliminate these large particles for recycling, Liu et al. processed used 316L powder without sieving and found that the tensile properties of the parts exhibited decreased strength and elongation which were attributed to laser spatter contamination of the powder-bed. From both of these studies, it is clear that laser spatter's large size allows for it to settle into the powder-bed thus compromising the reusability of the powder. These large particles as well as the formation of oxides on their surfaces may be a reason why researchers often find a coarsening particle size distribution and increase in oxygen content when performing recycling studies for various materials [23–25].

Although characterization of laser spatter has been performed in the aforementioned studies, more in-depth research needs to be conducted to rigorously understand the properties of laser spatter and its potential impact on the SLM process. Since laser spatter and condensate are coupled, characterization of condensate is also necessary, which, to our knowledge, has yet to be considered in the SLM community. Therefore, this study characterizes heat-affected powder in an attempt to understand how 304L stainless steel evolves with reuse during the SLM process. The characterization performed highlights the morphological, chemical, and microstructural differences observed between virgin 304L and heat-affected powder, thereby providing explanations for the changes often observed by researchers in recycled powder

Experimental Methods

A Renishaw AM250 SLM machine was used for fabrication of parts whose sole purpose was to produce heat-affected powder for subsequent characterization. The AM250 is equipped with a 200W Nd-YAG 1070 nm pulsed laser that has a Gaussian beam intensity profile. To ensure minimal oxidation of the parts, the entire build chamber was rendered inert until a stabilized oxygen content below 1000 ppm was observed. During operation, a constant 400 ft^3/min

volumetric flow rate of argon crossflow was maintained across the build plate to serve as a shielding gas against oxidation and for adequate removal of melt pool ejecta from the path of the laser beam.

Since heat-affected powder is formed by the interaction of the laser beam with the powder-bed, increasing the area to be melted in each layer ultimately leads to a larger amount of spatter and condensate generation. Thus, in order to generate a significant amount of heat-affected powder for analysis, it was desired to utilize a large portion of the build area without requiring copious time and resources. Consequently, 50% of the substrate area was chosen as a means to fulfill these requirements where a 5x5 array of plates each 15 mm in height was selectively melted as illustrated in Figure 1.

The powder used in this study was argon gas-atomized 304L stainless steel purchased from LPW Technology with its chemical composition listed in Table 1. Before being inserted into the Renishaw AM250, all virgin powder was sieved using a 63 μm screen in an argon atmosphere for removal of aggregates, breakup of agglomerates, and minimization of oxygen introduction into the build chamber. Once loaded in the SLM machine, the powder was dispensed and spread across the substrate for assessment of layer uniformity.

Due to direction of the argon crossflow, the location immediately downstream of the build plate (Figure 1) becomes concentrated in laser spatter and condensate during part fabrication. For this reason, a powder sample was taken from this area (heat-affected powder) using a clean spatula, thereby excluding the unconsolidated powder in the powder bed. An additional sample was taken from one of the walls of the build chamber in attempt to obtain a highly concentrated sample of condensate material. Characterization of this sample was performed with the use of a scanning electron microscope (SEM) as well as energy-dispersive spectroscopy (EDS). In an attempt to separate laser spatter from condensate for characterization of each individually, the heat-affected

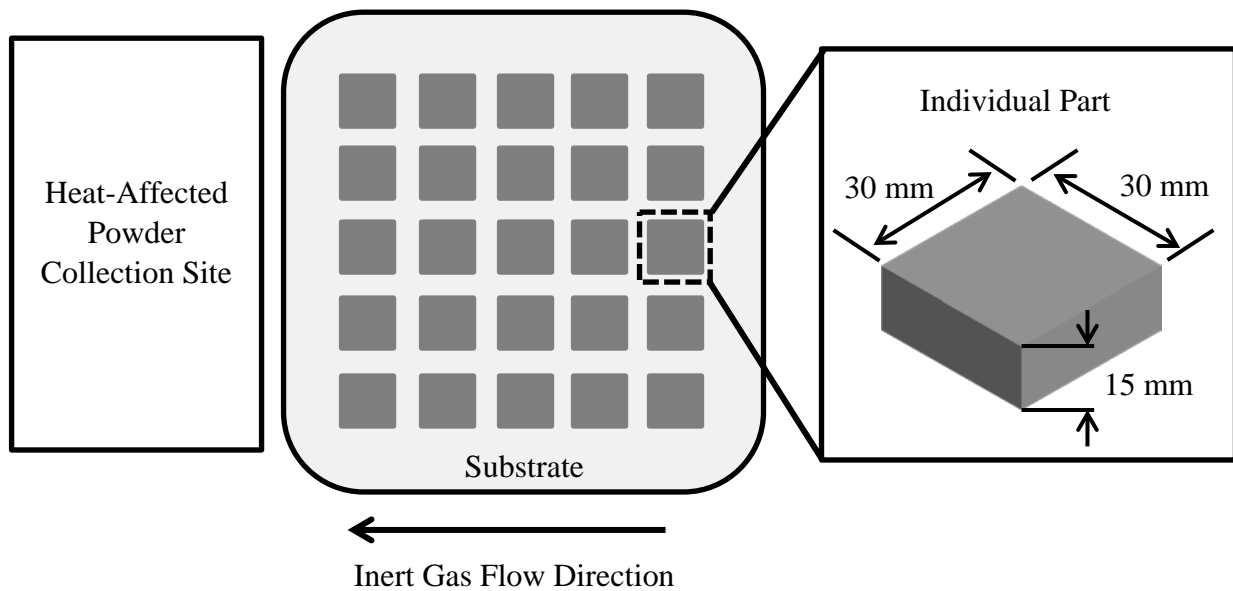


Figure 1. Illustration of the experimental setup of the build. The combined area of the parts for each layer corresponds to 50% of the substrate area.

powder was sieved using an ATM Sonic Sifter using 25 μm and 45 μm screens for separation into three size ranges, namely, -25 μm , +25 -45 μm , and +45 μm . Each size fraction was then homogenized using a Turbula T2C mixer to eliminate sampling bias and analyzed in regards to morphology, chemistry, and microstructure.

Table 1. Chemical composition of virgin 304L stainless steel powder.

	Element										
	C	Cr	Cu	Fe	Mn	N	Ni	O	P	S	Si
Wt %	0.018	18.4	< 0.1	Bal	1.4	0.06	9.8	0.02	0.012	0.005	0.63

Morphological characterization carried out in this study employed the use of three SEMs: Hitachi S4700, FEI Helios NanoLab 600, and an ASPEX 1020. While imaging and EDS were performed across all instruments, the automated feature analysis (AFA) capability of the ASPEX 1020 was employed for generation of particle size distributions and determination of particle shape using the circularity shape factor as outlined by Cox [26]. AFA allows the user to establish a region of interest on a sample and then measure specific properties of the encompassed features including projected area, perimeter, and chemistry. Each of the particle size distributions obtained was from at least 2500 particles to generate reliable distributions [27]. All number distributions were converted to a volume basis assuming a spherical shape for each particle.

Chemical characterization of each powder sample involved the use of EDS for an approximation of elemental concentration. To avoid possible discrepancies in the EDS results due to particle curvature [25], each powder sample was mounted in epoxy, ground, and polished to 0.05 μm using a small force in each step to minimize particle pullout. Before insertion into the SEM, an Au/Pd coating was applied to each mounted powder sample and electrically grounded with copper tape to eliminate charging and beam deflection. EDS measurements were taken at various locations on several particles for comparison of chemistry. Further use of EDS involved mapping across the polished surface of a large heat-affected powder particle for insight into potential segregation of Cr and Ni. Oxides on heat-affected powder were investigated by a focused-ion beam (FIB) for milling and imaging the oxide/metal interface.

For identification of phases present, a Panalytical X'Pert Pro Multi-Purpose Diffractometer was utilized to perform subsequent analysis using Rietveld refinement for quantification of the volume percentage of phases present.

Results and Discussion

Morphological Characterization

Electron micrographs of the -63 μm virgin 304L used for part fabrication as well as the heat-affected powder downstream of the build area sieved at various size fractions are shown in Figure 2. Although large particles greater than 100 μm clearly exist, it is apparent that particles below 25 μm exist as well. Thus, heat-affected powder is comprised of particles with a large size range, all of which have the potential to be redeposited on parts or in the powder bed. Particles larger than the base powder that fall onto parts can cause issues during fabrication including lack

of fusion due to the inability to be fully melted by the laser, and damage to the recoater mechanism affecting the powder-bed density. If redeposited in the powder bed and not subsequently melted, the size distribution of the unconsolidated powder will undoubtedly be altered. As a result, the deposition of large particles in the powder bed can contribute to the coarsening of powder with continual reuse. Although sieving may serve as an effective means towards removing these large particles, such a procedure will not be able to eliminate all heat-affected powder since it is composed of particles similar in size to virgin 304L.

Although aggregates are present in all size fractions, it is important to note that many of the particles exhibit a high degree of circularity when compared to the base powder. Thus, the cooling rate was low enough to allow surface tension forces to shape the molten material into spheres during flight. This is the reason why the particles in +45 μm size fraction appear to be the most circular of all the samples observed. Verification of this observation was made through the quantification of the particle shape through circularity. The average circularity for each sample is

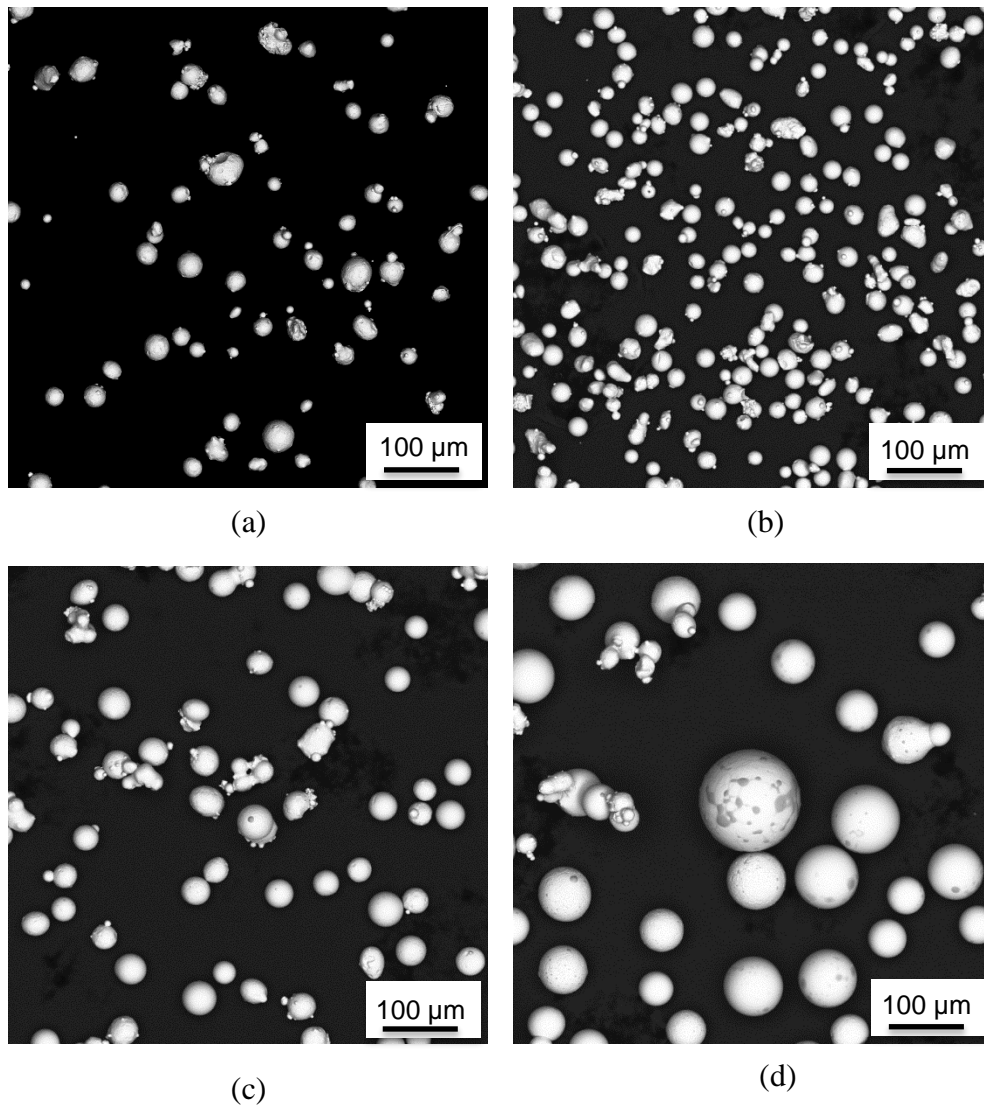


Figure 2. Heat-affected powder sieved at various size fractions taken with ASPEX SEM, including (a) Virgin 304L, (b) -25 μm , (c) +25/-45 μm , and (d) +45 μm .

tabulated in Table 2. The closer the circularity value is to unity, the more circular the geometry. The coarsest size fraction can be seen to have the highest circularity illustrating its sphericity in comparison to the other samples. Surprisingly, virgin 304L exhibits the lowest circularity even though no aggregates or agglomerates in the sample were noticed.

Table 2. A listing of the D10, D50, and D90 on a number and volume basis for each measured size distribution with incorporation of the minimum and maximum particle size. A comparison of shape using the circularity shape factor is also provided.

	Sample			
	Virgin 304L	-25 μm	+25 -45 μm	+45 μm
D _n 10 (μm)	16.1	16.9	31.4	46.1
D _n 50 (μm)	21.4	22.1	37.9	55.7
D _n 90 (μm)	31.4	29.0	46.1	78.2
D _v 10 (μm)	19.2	19.0	33.4	49.5
D _v 50 (μm)	27.5	25.5	40.8	66.7
D _v 90 (μm)	38.3	33.7	51	94.6
Minimum (μm)	0.3	1.8	10.2	20.3
Maximum (μm)	54.5	48.4	65.9	123.1
Circularity	0.81	0.89	0.83	0.90

Figure 3 gives the particle size distributions of each sample in number and volume representations. Information regarding the D10, D50, and D90 for the number and volume distributions is given in Table 2. Among the distributions shown, the virgin 304L has the highest number of fines present even when compared to the -25 μm size fraction. Since one of the main goals of sieving was to separate laser spatter from condensate, this result indicates that the presence of condensate in the region where the heat-affected powder was collected is either minimal or unable to be measured by AFA due to its small size of approximately 100 nm for mild steel. However, it is important to note that particles of this size were never observed in any of the micrographs taken of the heat-affected powder samples, with the smallest particle size measured being 1.8 μm . This could indicate that a significant amount of condensate generated is entrained in the argon flow across the build area and subsequently removed rather than depositing in the powder bed. A word of caution concerning this result is that the removal of condensate strongly depends on the inlet gas flow geometry and the magnitude of the flow during the process [18,20]. Therefore, this finding does not apply universally and should be investigated by each researcher to ensure adequate removal of laser byproduct for quality control.

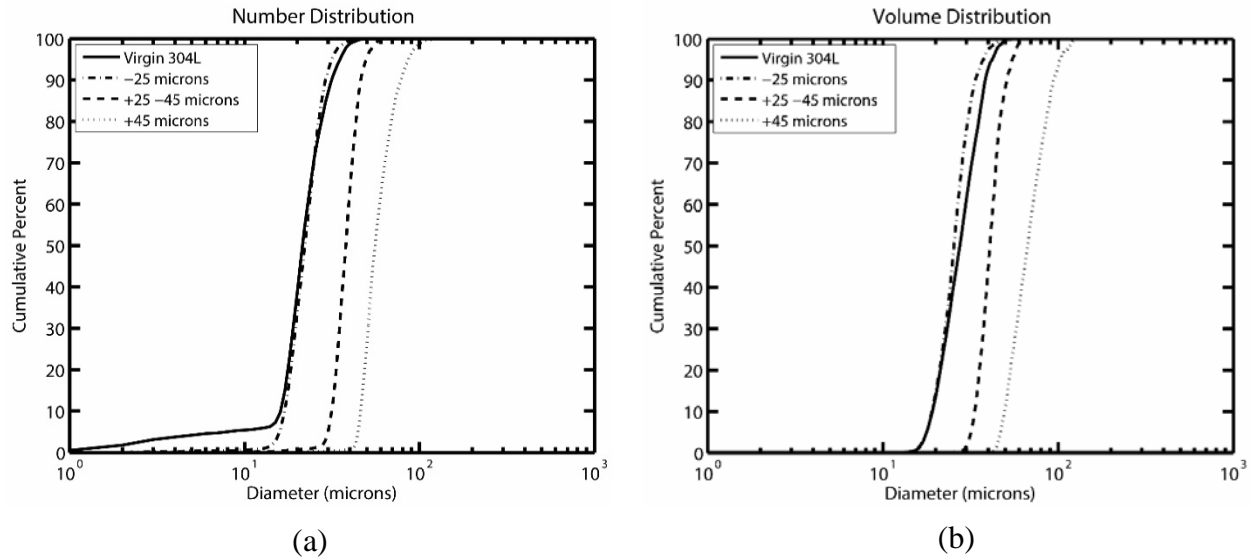


Figure 3. Particle size distributions of virgin 304L and size fractions of heat-affected powder in (a) number distribution and (b) volume distribution.

While condensate was not detected in the heat-affected powder collected downstream of the build area, images of the sample taken from the chamber wall can be seen in Figure 4, which reveals the appearance of powder similar in size to what is reported in literature regarding condensate as previously mentioned. As a consequence of its size, the powder agglomerates and loosely adheres to surfaces in the build chamber producing a thin film of material that collects on most surfaces in the build chamber during processing, and exhibits a blackened appearance. The relatively small size of condensate particles indicates that vaporization of material occurred while parts were being built and was immediately quenched in the chamber atmosphere.

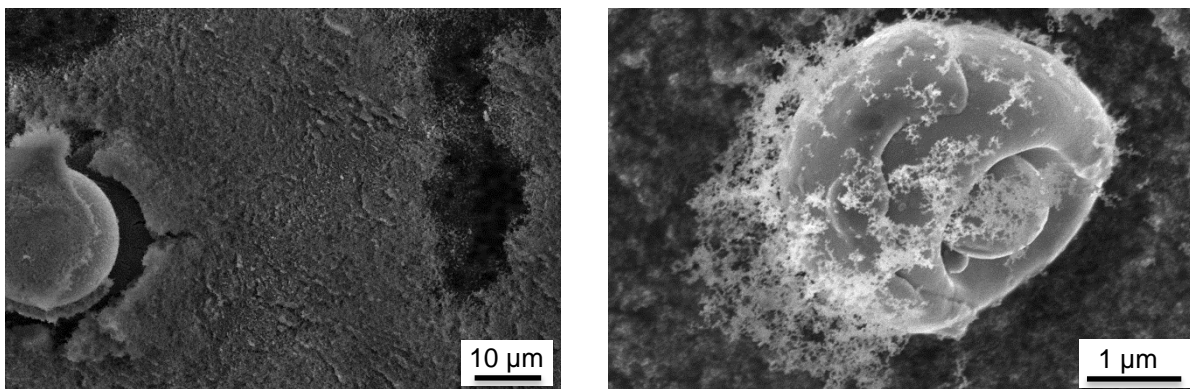


Figure 4. Images of a sample taken from the chamber wall after part fabrication showing heavy concentration of condensate.

Chemical Characterization

While Figure 2 illustrates the morphological differences between the base and heat-affected powder, it is obvious that the surfaces of some heat-affected particles contain dark regions

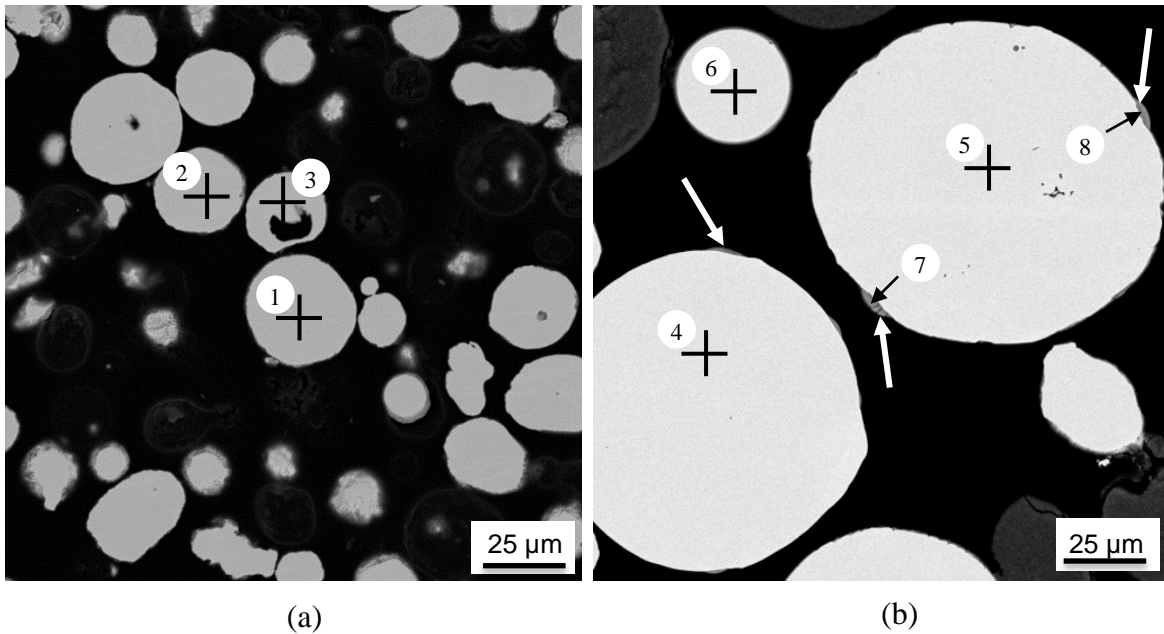


Figure 5. Electron micrographs of cross-sectioned (a) virgin 304L and (b) heat-affected powder. The white arrows indicate surface features present on heat-affected particles, and the black arrows represent the location of EDS performed on said regions.

indicative of a lower atomic number. Since the precursor powder does not contain such features, it was of interest to chemically identify these regions and provide rationale for their formation.

Identification of the chemical species present was performed by EDS in the ASPEX 1020. Rather than simply do a point EDS on the surface of particles, samples of virgin 304L and heat-affected powder were mounted in epoxy and cross-sectioned before insertion into the SEM. Figure 5 shows the powder cross-sections produced by mounting and polishing as well as the points of exposure for EDS measurement. Immediately noticeable are the previously observed structures (white arrows) present on the particle surfaces in Figure 5b where no distinct penetration into the underlying particle bulk is obvious. EDS measurements for each of the indicated locations are provided in Table 3. Given the uncertainty in EDS, the slight variability in the elemental concentrations in points 1 – 6 show no significant differences in bulk chemistry among the two powders. However, points 7 and 8 reveal a strong presence of Mn, Si, and O. Since Mn and Si are strong oxide formers and the observed features are located on the surface of the particles, these regions are most likely oxides that formed while the particles were in flight after being ejected from the melt pool. Simonelli [22] found a very similar result when studying 316L laser spatter formed during SLM. Chasoglou [28] also observed the same oxide island features on a water-atomized steel powder for use in powder metallurgy. After using XPS, it was concluded that these oxides contain Fe and Cr in addition to Mn and Si. For a more thorough characterization of the oxides present, a similar approach will need to be taken to enable a look into the bonding states of the elements present.

Table 3. EDS measurements at various locations on virgin powder and heat-affected particles.

Location	Element (Wt %)						
	Fe	Cr	Ni	Mn	O	C	Si
1	64.7	22.3	7.0	2.5	1.9	1.3	0.3
2	63.0	22.0	7.9	2.1	3.3	1.5	0.3
3	63.4	21.4	7.5	3.2	2.3	1.7	0.5
4	65.3	21.1	7.5	2.7	1.6	1.6	0.2
5	64.2	21.6	6.7	3.0	2.5	1.5	0.5
6	63.0	21.6	8.4	3.0	2.2	1.4	0.4
7	2.6	7.7	0.5	17.3	53.4	7.1	11.3
8	1.5	5.9	0.5	9.0	61.6	5.8	15.8

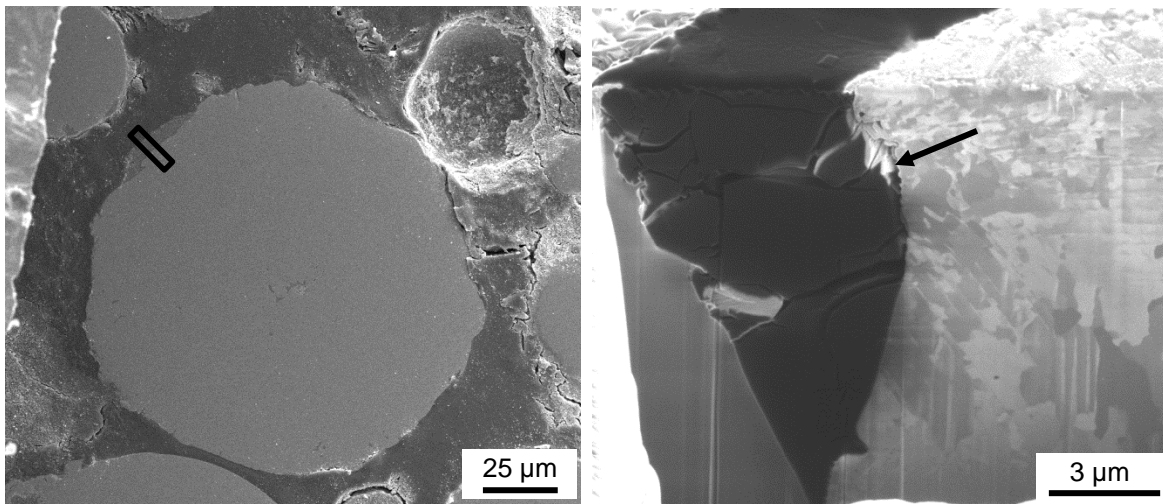


Figure 6. (a) Electron micrograph of a polished heat-affected particle with a large oxide on its surface where the black rectangle indicates a region for subsequent FIB analysis, and (b) FIB image of the oxide/metal interface, as denoted by the black arrow.

While the presence of oxides on the surfaces of heat-affected particles is reasonable due to the 1000 ppm oxygen content of the build atmosphere during operation, the formation of islands of oxides is less intuitive and deserves an explanation. The current theory regarding oxidation of metals can be categorized into four stages: induction, nucleation, growth, and coalescence [29,30]. Induction is the time preceding nucleation of oxide islands where the dissociation of oxygen molecules and subsequent chemisorption of oxygen occur on the metal surface. Once a sufficient oxygen concentration is reached, stable oxide nuclei form and grow. During the growth stage, the oxides will merge and coalesce becoming larger to eventually create a continuous film of oxide.

The oxide islands in Figure 5b seem to follow this four stage progression where the features were in the growth phase until the particle cooled. One important detail of this reaction sequence is the penetration of oxide into the underlying metal as a result of oxygen diffusion into the metal lattice. For observation of consumption of the metal particle by the oxide, a FIB was used to

generate a cross-section of the oxide/metal interface of a polished heat-affected particle. Figure 6a shows the heat-affected particle selected as well as the region of interest denoted by a black rectangle. The oxide/metal interface in Figure 6b clearly shows a curvature meaning the oxide consumed a portion of the metal, a result that is explained in detail by Zhou [30].

Due to the relatively slow cooling rate of large particles, the developed microstructure could possibly chemically segregate as a consequence of solute rejection from the melt. Depending on the solidification mode of the stainless steel, the chromium and nickel will either be retained in the solid or rejected ahead of the solidification front. Although such a result is uncommon for high cooling rates, solute redistribution is a common occurrence in alloys as the cooling rate decreases. In order to evaluate if microsegregation of elements occurs in the larger particles, EDS maps of cross-sectioned particle surface were generated. The EDS maps generated for a large heat-affected particle can be seen in Figure 7. Based on the results, microsegregation could not be detected given the resolution limit of EDS.

The chemistry of the condensate was also investigated with EDS for insight into possible elemental vaporization. For this investigation, the powder sample collected from the chamber wall was examined since it was found that the powder collected there has a concentration of condensate relative to the heat-affected powder collected downstream of the build area. In order to avoid the effects of interaction volume skewing the measurements, a particle with a large amount of agglomerated condensate was found and analyzed, as depicted in Figure 8. The EDS results in Table 4 reveal a significant amount of each element found in the base powder with the exception of Ni. This indicates vaporization of all the elements present within the melt pool suggesting that a large amount of superheat is generated during processing. Although it is still not clear whether condensate is deposited inside the build area since none was found in the heat-affected powder sample, this result does show vaporization of all elements occurred. Therefore, potential chemistry modifications may need to be made to the precursor powder to have more control over part chemistry.

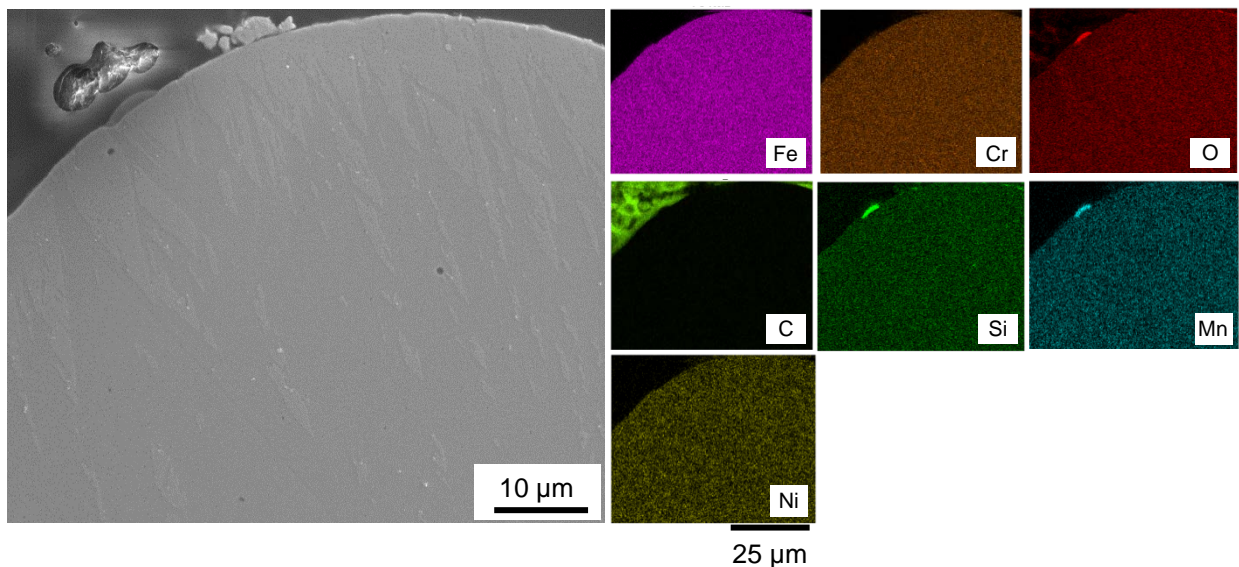


Figure 7. EDS maps of a large heat-affected powder particle showing no evidence of microsegregation.

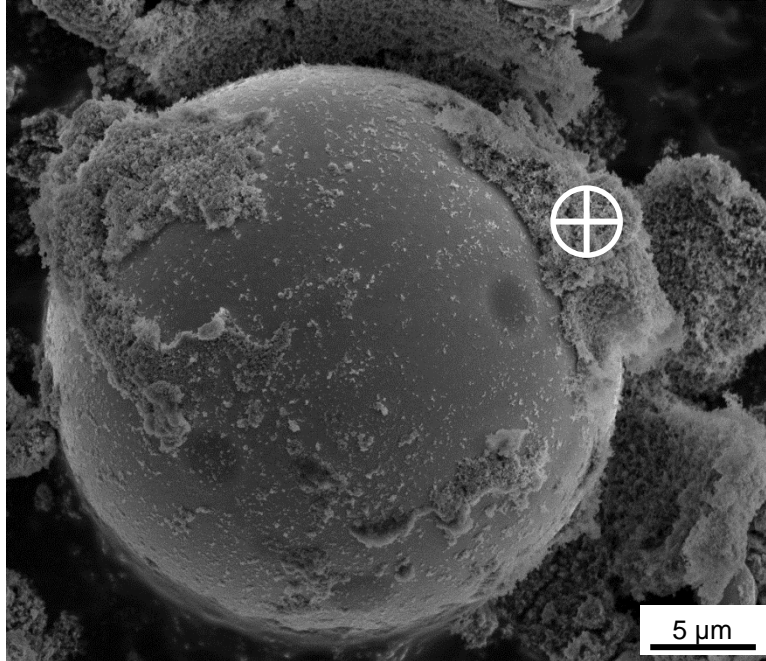


Figure 8. Heat-affected particle with condensate on its surface. The white cross-hairs indicate the location of EDS measurement.

Table 4. EDS results of condensate showing a large amount of all elements present.

	Element						
	C	O	Si	Cr	Mn	Fe	Ni
Wt %	12.52%	17.37%	16.53%	12.53%	5.99%	32.03%	3.02%

Microstructural Characterization

Identification of the phases present within the powder samples was performed through XRD for virgin 304L, heat-affected powder and its size fractions. Figure 9 shows the obtained diffraction patterns indicating a strong presence of austenite and delta ferrite in all analyzed samples. Virgin 304L is nearly pure austenite while heat-affected powder shows significant delta ferrite. Moreover, the amount of each phase varies as a function of the size fraction where the primary austenite peak at 44° is less prominent as the particle size increases indicating an increase in delta ferrite. Quantification of the XRD diffraction patterns was performed through Rietveld refinement and can be seen graphically in Figure 10 accompanied by the tabulated results in Table 5. Since the chemistry of each fraction is nearly the same as previously confirmed by EDS, the observed trend is indicative of a cooling rate difference between the smallest and largest particles. Therefore, further investigation must include the estimation of cooling rate as a function of particle size to view this correlation.

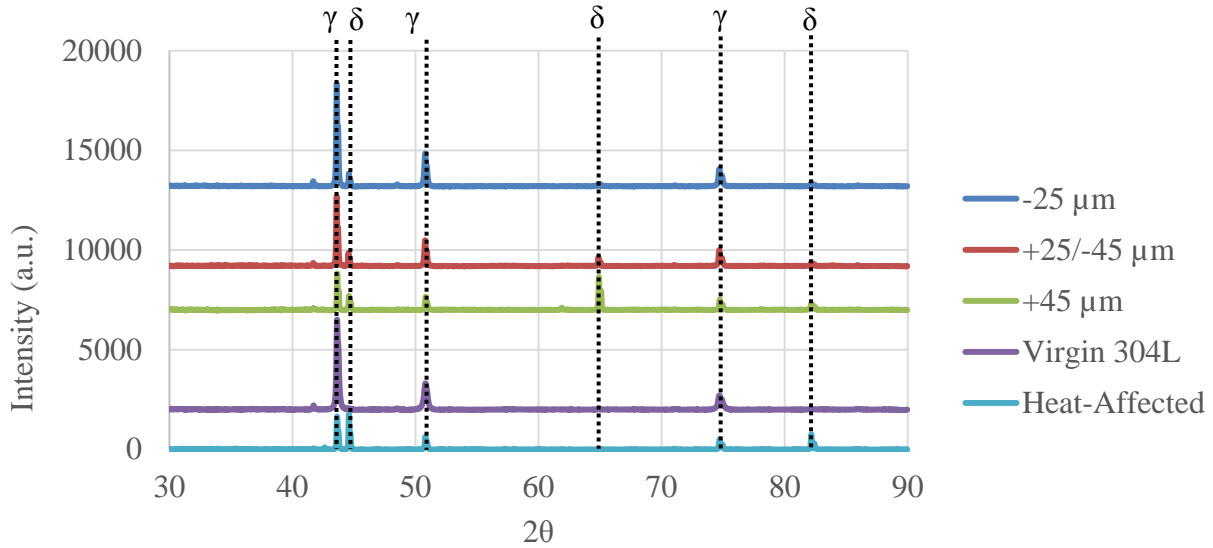


Figure 9. XRD diffraction patterns of heat-affected powder and its size fractions compared to virgin 304L.

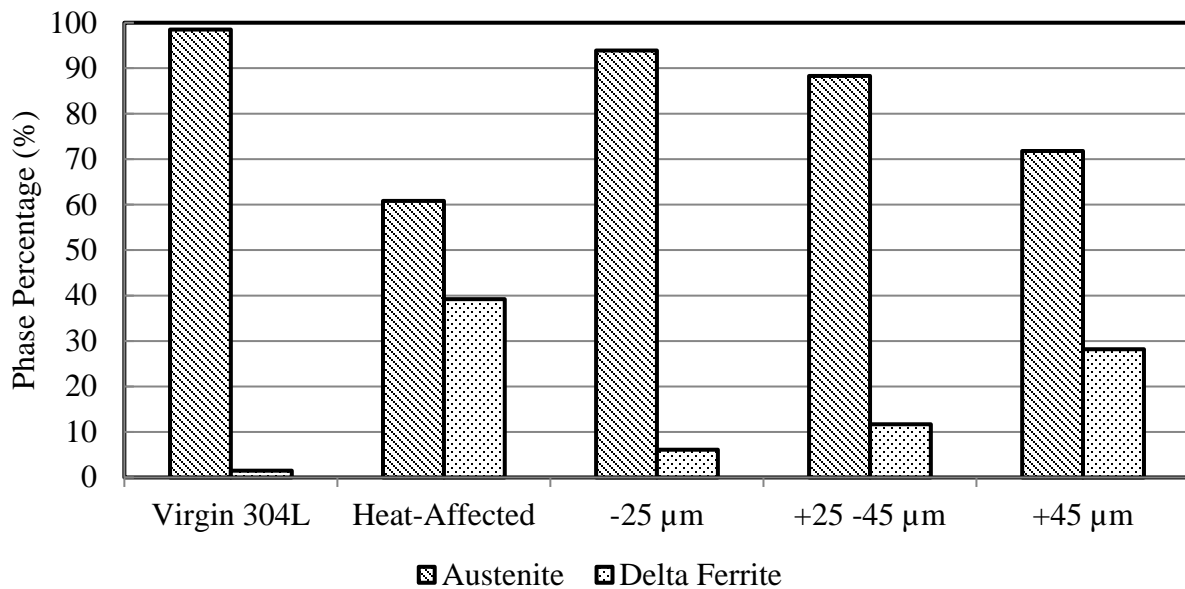


Figure 10. Quantification of XRD diffraction patterns using Rietveld refinement illustrating the dependence of delta ferrite formation on the particle size.

Table 5. Quantification of austenite and delta ferrite fractions for heat-affected powder and its various size fractions in comparison to virgin 304L.

	Sample				
	Virgin 304L	Heat-Affected	-25 μm	+25 -45 μm	+45 μm
Austenite (%)	98.5	60.8	93.9	88.3	71.8
Delta Ferrite (%)	1.5	39.2	6.1	11.7	28.2

The difference in the relative proportion of austenite and delta ferrite formation can be explained through the determination of solidification mode, or the sequence of phase transformations that occurs during solidification and subsequent cooling as a solid. Since chromium and nickel are strong delta ferrite and austenite stabilizers, respectively, the solidification mode in stainless steels is often determined through the ratio of chromium to nickel equivalencies (Cr_{eq}/Ni_{eq}). A listing of the available methods for evaluation of Cr_{eq}/Ni_{eq} is given by Kiorinko et al. [31]. In general, there exist four types of solidification modes [32]:

1. A mode: $L \rightarrow L + \gamma \rightarrow \gamma$ for $Cr_{eq}/Ni_{eq} < 1.25$
2. AF mode: $L \rightarrow L + \gamma \rightarrow L + \delta + \gamma \rightarrow \gamma + \delta \rightarrow \gamma$ for $1.25 < Cr_{eq}/Ni_{eq} < 1.48$
3. FA mode: $L \rightarrow L + \delta \rightarrow L + \delta + \gamma \rightarrow \gamma + \delta \rightarrow \gamma$ for $1.48 < Cr_{eq}/Ni_{eq} < 1.95$
4. F mode: $L \rightarrow L + \delta \rightarrow \delta \rightarrow \delta + \gamma \rightarrow \gamma$ for $Cr_{eq}/Ni_{eq} > 1.95$

Using the chemistry of the virgin powder provided by LPW Technology (Table 1) and calculating the Cr_{eq}/Ni_{eq} using the Hull expression, we find that 304L will solidify as primary ferrite and then austenite (FA). At high cooling rates, the solid-state transformation of delta ferrite to austenite is hindered thus allowing retention of the delta ferrite phase. However, at even higher cooling rates approaching 10^5 K/s, it is possible for the solidification mode to change from FA to AF as a result of a sufficient amount of undercooling. Since virgin 304L is gas-atomized where typical cooling rates are on the order of 10^5 K/s, it is reasonable that 304L is primarily austenite. If the percentage of delta ferrite decreases with increasing cooling rate, it is reasonable to assume that the smaller size fractions ($\sim 45 \mu\text{m}$) are approaching an AF solidification mode whereas the large particles are solidifying as FA.

A few studies [33,34] have demonstrated that powder properties can influence phase formation in as-built components. While the influence of particle microstructure on part properties is out of the scope of this paper, it is important to understand the formation of delta ferrite indicates the presence of heat-affected powder. Thus, phase quantification could prove as a viable approach towards assessing the degree of which a powder has been used.

Conclusions

In this study, the morphological, chemical, and microstructural properties of heat-affected powder were investigated for insight into the expected changes that are to occur as a result of recycling 304L stainless steel in the SLM process. While previous studies primarily focus on laser spatter, emphasis in the current study was placed on the combination of laser spatter and condensate for a more comprehensive characterization of ejecta originating from the melt pool. Clear identification of both laser spatter and condensate was accomplished by collecting two samples: heat-affected powder downstream of the build area, and a sample from the wall of the chamber after building parts. The collected heat-affected powder was found to be primarily laser spatter, suggesting that most of the condensate does not deposit in the build area. However, such a conclusion is highly dependent on the magnitude of argon crossflow employed as well as the geometry of the build chamber and inlet gas manifold. Thus, each researcher must study the flow inside the build chamber for insight into condensate deposition inside the build chamber. The size of laser spatter particles was found to exist across a large size range where, once ejected, deposition into the build area is possible, potentially compromising powder reuse. Although the size range is

large, the average circularity of the laser spatter in each size fraction was found to be greater than that of that the base powder. It is important to note that aggregates were found to exist as a consequence of particles merging while molten.

Investigation of powder chemistry led to the observation of oxide islands on laser spatter. These oxides are rich in Mn and Si, which are strong oxide formers. Further analysis revealed that these oxides nucleate and grow on the surfaces of particles. Depending on the growth rate of the oxides, the coalescence of these islands will vary, producing oxides of various size. EDS also allowed for identification of the chemical species available in condensate powder. Based on these results, it is clear that the condensate is comprised of appreciable amounts of all alloying elements present in the base powder, providing evidence for large superheat in the melt pool.

Microstructural analysis of the heat-affected size fractions and virgin 304L through XRD showed varying amounts of austenite and delta ferrite. In general, it was found that the percentage of delta ferrite increased with increasing particle size. These results were attributed to the large difference in cooling rates experienced by the large and small particles, enabling the switch from FA to AF solidification mode through an increased undercooling. Since delta ferrite is a marker of heat-affected powder, phase identification is a viable technique for distinguishing between virgin and used 304L powder.

The results from this study show that 304L will change as it is reused in SLM. Even though the degree of its reusability has yet to be determined, changes in the properties of recycled powder can now be better understood with knowledge of the mechanisms responsible for powder degradation. This investigation shows that not only the size distribution of the unconsolidated powder will be altered with continual reuse, but also its chemistry due to the formation of oxides. The effects of such changes in powder properties on part quality will be evaluated in the future to assess the reusability of 304L in SLM.

Acknowledgements

This work was funded by Honeywell Federal Manufacturing & Technologies under Contract No. DE-NA0002839 with the U.S. Department of Energy. The United States Government retains and the publisher, by accepting the article for publication, acknowledges that the United States Government retains a nonexclusive, paid up, irrevocable, world-wide license to publish or reproduce the published form of this manuscript, or allow others to do so, for the United States Government purposes.

References

- [1] A.T. Sutton, C.S. Kriewall, M.C. Leu, J.W. Newkirk, Powder characterisation techniques and effects of powder characteristics on part properties in powder-bed fusion processes, *Virtual Phys. Prototyp.* 12 (2017) 3–29. doi:10.1080/17452759.2016.1250605.
- [2] J.P. Kruth, G. Levy, F. Klocke, T.H.C. Childs, Consolidation phenomena in laser and powder-bed based layered manufacturing, *CIRP Ann. - Manuf. Technol.* 56 (2007) 730–759. doi:10.1016/j.cirp.2007.10.004.
- [3] N. Guo, M.C. Leu, Additive manufacturing: Technology, applications and research needs, *Front. Mech. Eng.* 8 (2013) 215–243. doi:10.1007/s11465-013-0248-8.

- [4] L. Thijs, F. Verhaeghe, T. Craeghs, J. Van Humbeeck, J.P. Kruth, A study of the microstructural evolution during selective laser melting of Ti-6Al-4V, *Acta Mater.* 58 (2010) 3303–3312. doi:10.1016/j.actamat.2010.02.004.
- [5] B. Ahuja, A. Schaub, M. Karg, M. Lechner, M. Merklein, M. Schmidt, Developing LBM Process Parameters for Ti-6Al-4V Thin Wall Structures and Determining the Corresponding Mechanical Characteristics, *Phys. Procedia.* 56 (2014) 90–98. doi:10.1016/j.phpro.2014.08.102.
- [6] R. Li, J. Liu, Y. Shi, M. Du, Z. Xie, 316L stainless steel with gradient porosity fabricated by selective laser melting, *J. Mater. Eng. Perform.* 19 (2010) 666–671. doi:10.1007/s11665-009-9535-2.
- [7] I. Tolosa, F. Garcíandía, F. Zubiri, F. Zapirain, A. Esnaola, Study of mechanical properties of AISI 316 stainless steel processed by “selective laser melting”, following different manufacturing strategies, *Int. J. Adv. Manuf. Technol.* 51 (2010) 639–647. doi:10.1007/s00170-010-2631-5.
- [8] Z. Wang, K. Guan, M. Gao, X. Li, X. Chen, X. Zeng, The microstructure and mechanical properties of deposited-IN718 by selective laser melting, *J. Alloys Compd.* 513 (2012) 518–523. doi:10.1016/j.jallcom.2011.10.107.
- [9] C. Yan, L. Hao, A. Hussein, D. Raymont, Evaluations of cellular lattice structures manufactured using selective laser melting, *Int. J. Mach. Tools Manuf.* 62 (2012) 32–38. doi:10.1016/j.ijmactools.2012.06.002.
- [10] S.A. Khairallah, A. Anderson, Mesoscopic simulation model of selective laser melting of stainless steel powder, *J. Mater. Process. Technol.* 214 (2014) 2627–2636. doi:10.1016/j.jmatprotec.2014.06.001.
- [11] a. V. Gusarov, I. Yadroitsev, P. Bertrand, I. Smurov, Heat transfer modelling and stability analysis of selective laser melting, *Appl. Surf. Sci.* 254 (2007) 975–979. doi:10.1016/j.apsusc.2007.08.074.
- [12] F. Verhaeghe, T. Craeghs, J. Heulens, L. Pandelaers, A pragmatic model for selective laser melting with evaporation, *Acta Mater.* 57 (2009) 6006–6012. doi:10.1016/j.actamat.2009.08.027.
- [13] D. Gu, Y. Shen, Balling phenomena during direct laser sintering of multi-component Cu-based metal powder, *J. Alloys Compd.* 432 (2007) 163–166. doi:10.1016/j.jallcom.2006.06.011.
- [14] M. Agarwala, D. Bourell, J. Beaman, H. Marcus, J. Barlow, Direct selective laser sintering of metals, *Rapid Prototyp. J.* 1 (1995) 26–36. doi:10.1108/13552549510078113.
- [15] M.J. Zhang, G.Y. Chen, Y. Zhou, S.C. Li, H. Deng, Observation of spatter formation mechanisms in high-power fiber laser welding of thick plate, *Appl. Surf. Sci.* 280 (2013) 868–875. doi:10.1016/j.apsusc.2013.05.081.
- [16] Y. Kawahito, M. Mizutani, S. Katayama, High quality welding of stainless steel with 10 kW high power fibre laser, *Sci. Technol. Weld. Join.* 14 (2009) 288–294. doi:10.1179/136217108X372531.
- [17] A.F.H. Kaplan, J. Powell, Spatter in laser welding, *J. Laser Appl.* 23 (2011) 1–7.
- [18] A. Ladewig, G. Schlick, M. Fisser, V. Schulze, U. Glatzel, Influence of the shielding gas flow on the removal of process by-products in the selective laser melting process, *Addit. Manuf.* 10 (2016) 1–9. doi:10.1016/j.addma.2016.01.004.
- [19] Y. Liu, Y. Yang, S. Mai, D. Wang, C. Song, Investigation into spatter behavior during selective laser melting of AISI 316L stainless steel powder, *Mater. Des.* 87 (2015) 797–806.

- doi:10.1016/j.matdes.2015.08.086.
- [20] B. Ferrar, L. Mullen, E. Jones, R. Stamp, C.J. Sutcliffe, Gas flow effects on selective laser melting (SLM) manufacturing performance, *J. Mater. Process. Technol.* 212 (2012) 355–364. doi:10.1016/j.jmatprotec.2011.09.020.
- [21] P.Y. Shcheglov, a V Gumenyuk, I.B. Gornushkin, M. Rethmeier, V.N. Petrovskiy, Vapor–plasma plume investigation during high-power fiber laser welding, *Laser Phys.* 23 (2013) 16001. doi:10.1088/1054-660X/23/1/016001.
- [22] M. Simonelli, C. Tuck, N.T. Aboulkhair, I. Maskery, I. Ashcroft, R.D. Wildman, R. Hague, A Study on the Laser Spatter and the Oxidation Reactions During Selective Laser Melting of 316L Stainless Steel, Al-Si10-Mg, and Ti-6Al-4V, *Metall. Mater. Trans. A.* (2015). doi:10.1007/s11661-015-2882-8.
- [23] V. Seyda, N. Kaufmann, C. Emmelmann, Investigation of Aging Processes of Ti-6Al-4 V Powder Material in Laser Melting, *Phys. Procedia.* 39 (2012) 425–431. doi:10.1016/j.phpro.2012.10.057.
- [24] L.C. Ardila, F. Garcíandia, J.B. González-Díaz, P. Álvarez, a Echeverria, M.M. Petite, R. Deffley, J. Ochoa, Effect of IN718 Recycled Powder Reuse on Properties of Parts Manufactured by Means of Selective Laser Melting, *Phys. Procedia.* 56 (2014) 99–107. doi:10.1016/j.phpro.2014.08.152.
- [25] J.A. Slotwinski, E.J. Garboczi, P.E. Stutzman, C.F. Ferraris, S.S. Watson, M.A. Peltz, Characterization of metal powders used for additive manufacturing, *J. Res. Natl. Inst. Stand. Technol.* 119 (2014) 460–493. doi:10.6028/jres.119.018.
- [26] E. Cox, A method of assigning numerical and percentage values to the degree of roundness of sand grains, *J. Paleontol.* 1 (1927) 179–183. <http://www.jstor.org/stable/10.2307/1298056>.
- [27] E. Vigneau, C. Loisel, M.F. Devaux, P. Cantoni, Number of particles for the determination of size distribution from microscopic images, *Powder Technol.* 107 (2000) 243–250. doi:10.1016/S0032-5910(99)00192-8.
- [28] D. Chasoglou, E. Hryha, M. Norell, L. Nyborg, Characterization of surface oxides on water-atomized steel powder by XPS/AES depth profiling and nano-scale lateral surface analysis, *Appl. Surf. Sci.* 268 (2013) 496–506. doi:10.1016/j.apsusc.2012.12.155.
- [29] R.K. Hart, J.K. Maurin, P.S. Division, The nucleation and growth on aluminum* of oxide islands, *Surf. Sci.* 20 (1970) 285–303.
- [30] G. Zhou, Nucleation-induced kinetic hindrance to the oxide formation during the initial oxidation of metals, *Phys. Rev. B - Condens. Matter Mater. Phys.* 81 (2010) 1–7. doi:10.1103/PhysRevB.81.195440.
- [31] P. Korinko, S. Malene, Considerations for the weldability of types 304L and 316L stainless steel, *J. Fail. Anal. Prev.* 1 (2001) 61–68. doi:10.1007/BF02715336.
- [32] J.W. Fu, Y.S. Yang, J.J. Guo, W.H. Tong, Effect of cooling rate on solidification microstructures in AISI 304 stainless steel, *Mater. Sci. Technol.* 24 (2008) 941–944. doi:10.1179/174328408X295962.
- [33] T. Starr, K. Rafi, B. Stucker, C. Scherzer, Controlling phase composition in selective laser melted stainless steels, in: *Proc. Solid Free. Fabr. Symp.*, 2012: pp. 439–446.
- [34] L.E. Murr, E. Martinez, J. Hernandez, S. Collins, K.N. Amato, S.M. Gaytan, P.W. Shindo, Microstructures and properties of 17-4 PH stainless steel fabricated by selective laser melting, *J. Mater. Res. Technol.* 1 (2012) 167–177. doi:10.1016/S2238-7854(12)70029-7.